



Original Research

Synergistic effects of polydopamine-coated reduced graphene oxide on osteogenesis and anti-inflammation in periodontitis

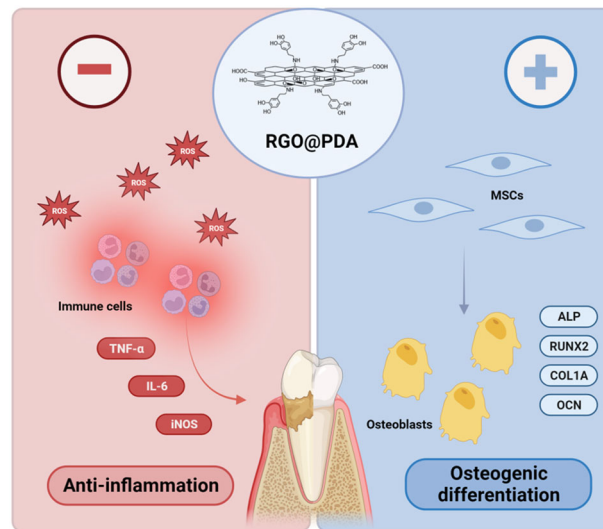
Xiaoge Jiang¹ · Xinyi Chen¹ · Qiming Li¹ · Xinyi Li¹ · Kaiwen Zhang¹ · Jiazhen Jiang¹ · Xinrui Men¹ · Wei-Cho Chiou¹ · Song Chen¹

Received: 14 March 2025 / Accepted: 22 May 2025
© The Author(s) 2025

Abstract

Owing to its extremely high prevalence and the distressing consequence of tooth loss, periodontitis has attracted substantial research attention. In light of these conditions, graphene-based biomaterials have emerged as a potentially promising approach for periodontal regeneration. This study focuses on the synthesis of polydopamine-coated reduced graphene oxide (RGO@PDA), designed to harness the anti-inflammatory properties of dopamine and the osteogenic potential of graphene oxide for synergistic periodontitis treatment. RGO@PDA was synthesized through a 12-h magnetic stirring process of graphene oxide and dopamine at room temperature. This water-dispersible and biocompatible compound demonstrated remarkable efficacy in enhancing osteogenic differentiation in rat bone mesenchymal stem cells (rBMSCs), evidenced by increased alkaline phosphatase activity, mineralization, and the upregulation of osteogenic genes and proteins. Furthermore, RGO@PDA showed significant capabilities in scavenging reactive oxygen species (ROS) and reducing proinflammatory factor expression. In vivo experiments revealed that RGO@PDA not only alleviated periodontal inflammation but also promoted alveolar bone repair in periodontitis-afflicted rats. These findings underscore RGO@PDA's dual anti-inflammatory and osteogenic effects, highlighting its potential as a transformative treatment for periodontitis.

Graphical Abstract



These authors contributed equally: Xiaoge Jiang, Xinyi Chen

✉ Song Chen
songchen882002@hotmail.com

¹ State Key Laboratory of Oral Diseases & National Center for

Stomatology & National Clinical Research Center for Oral Diseases & Dept. of Orthodontics, West China Hospital of Stomatology, Sichuan University, Chengdu, Sichuan, China

Keywords Graphene oxide · Polydopamine · Osteogenesis · Anti-inflammation · Periodontitis

1 Introduction

Periodontitis, a chronic inflammatory condition affecting a significant portion of the global population, leads to the progressive deterioration of soft tissue and bone support, culminating in irreversible tooth loss [1, 2]. Beyond its localized impact, periodontitis has been increasingly associated with systemic conditions such as diabetes, cardiovascular diseases, and chronic obstructive pulmonary disease [3–5]. Despite its prevalence and severity, current treatment strategies, including subgingival scaling, local and systemic pharmacotherapy, and various surgical interventions, fall short of achieving true tissue regeneration. These approaches primarily aim to control disease progression rather than restore lost periodontal structures [6]. Furthermore, they are fraught with limitations: subgingival instrumentation often fails to completely eradicate pathogenic biofilms, surgical procedures carry inherent risks of infection, and prolonged antibiotic use may foster microbial resistance [7–9]. It is widely recognized that oral periodontal pathogenic bacteria in dental plaque initiate the disease, triggering a host immune response characterized by the upregulation of proinflammatory factors and reactive oxygen species (ROS), ultimately leading to periodontal tissue destruction and alveolar bone loss [10]. These challenges emphasize the critical need for innovative therapies that not only stop disease progression but also promote functional periodontal regeneration, addressing both inflammation and osteogenesis of periodontitis.

As an emerging biomaterial, graphene-based materials have shown great potential in numerous research fields, including drug delivery, biosensors, bioimaging, photothermal therapy, and tissue engineering [11–15]. Graphene, composed of carbon atoms arranged in hexagonal lattices, exhibits extraordinary physical properties [16]. Derived from graphene, graphene oxide (GO) is characterized by its oxygen-rich structure, featuring hydroxyl and epoxide groups on its surface and carboxyl groups at its edges [17]. These functional groups enable GO to anchor various metallic nanoparticles and bioactive molecules, thereby enhancing its versatility [18]. GO and its derivatives have shown promise in tissue engineering due to their antimicrobial properties, low cytotoxicity, and regenerative capabilities [19–23]. Notably, studies have revealed that GO alone can stimulate the self-renewal and osteogenic differentiation of stem cells [24, 25]. Additionally, combining GO with osteoinductive materials like calcium phosphates has been shown to synergistically enhance the differentiation of human mesenchymal stem cells [26]. These findings

collectively underscore the immense potential of GO and its derivatives in advancing periodontal regeneration.

While the functional groups of GO confer hydrophilicity, enabling extensive modifications and diverse applications, they also contribute to its instability [27, 28]. This instability often manifests as a color change in GO colloidal suspensions from light brown to black, due to spontaneous reactions even under ambient conditions. Reduced graphene oxide (RGO) overcomes this limitation, offering improved structural stability [29]. The reduction degree of RGO can be precisely controlled by adjusting reaction parameters, such as the type of reducing agent and temperature, allowing for a tailored balance between surface functional groups and material properties. This balance not only meets the multifunctional demands of advanced materials but also provides a critical foundation for the development of high-performance composites, enhancing RGO's versatility for innovative applications [30].

Dopamine (DA) is a structurally simple, small-molecule compound synthesized through specific enzymatic reactions from L-tyrosine. Its synthesis begins with the conversion of L-tyrosine to 3,4-dihydroxy-L-phenylalanine (L-DOPA) under the action of tyrosine hydroxylase. Subsequently, L-DOPA undergoes decarboxylation catalyzed by DOPA decarboxylase, ultimately forming DA [31]. Notably, when a substrate is immersed in a dilute aqueous DA solution under alkaline conditions, DA undergoes self-polymerization and can adhere to virtually any substrate surface, forming a uniform and thin polydopamine (PDA) film [32]. This property endows it with broad application potential in materials science and biomedical fields. Beyond its adhesive qualities, DA has also demonstrated significant anti-inflammatory potential. Several researches indicate that DA can elevate intracellular cAMP levels, inhibit inflammatory pathways through D1 receptors, and thereby exert anti-inflammatory effects [33, 34]. Additionally, DA acts as an effective scavenger of reactive oxygen species (ROS), primarily due to the catechol groups in its chemical structure, further highlighting its therapeutic potential [35, 36].

Given the osteogenic potential of RGO and the anti-inflammatory properties of DA, we hypothesize that polydopamine-coated RGO could integrate the advantages of both materials, offering an effective solution for the treatment of periodontitis. In this study, we successfully synthesized polydopamine-coated reduced graphene oxide (RGO@PDA) through 12 h of magnetic stirring. Comprehensive *in vitro* experiments were conducted to evaluate its biocompatibility, osteogenic capacity, ROS scavenging ability, and anti-inflammatory effects. Additionally, *in vivo*

studies were performed by injecting RGO@PDA into the subgingival sulcus of rats with periodontitis. The results demonstrate the significant potential of RGO@PDA as an innovative therapeutic strategy for periodontitis, holding promise for breakthroughs in clinical treatment.

2 Materials and methods

2.1 Synthesis of RGO@PDA

Single-layer GO was purchased from Macklin (China). Dopamine hydrochloride (DA·HCl, purity >98%) was purchased from Aladdin (China). Briefly, The GO was dispersed by sonication for 30 min under low temperature. Then the dispersed GO and DA were dissolved in Tris-HCl buffer (10 mM, pH 8.5, adjusted by NaOH). To obtain the PDA-coated RGO, the mixture was magnetically stirred for 12 h at room temperature. The solution was then centrifuged at 6000 rpm for 10 min, and the supernatant was discarded, and the resultant mixture was washed three times with deionized water to remove the unpolymerized DA using centrifugation at room temperature. The final concentration of GO was 1 mg/ml, and the DA concentrations were 1 mg/ml, 2 mg/ml, 5 mg/ml, and 10 mg/ml, respectively. According to different DA/GO ratios, we described different samples as RGO-PDA-1, RGO-PDA-2, RGO-PDA-5, and RGO-PDA-10.

2.2 Characterization of RGO@PDA

The RGO@PDA solutions with different DA/GO feeding ratios were left to stand at room temperature for 30 min, and photographs were taken and recorded at two time points, 0 min and 30 min, respectively to test the water dispersion. The shape and morphologies of GO and RGO@PDA were observed by making use of a scanning electron microscope (SEM; Gemini 300, Germany) and a transmission electron microscope (TEM; Hitachi, Japan). The chemical states of the materials were investigated by Fourier transform infrared spectroscopy (FT-IR; NICOLET iS50, USA), Raman spectroscopy (LabRAM HR Evolution, France), and X-ray photoelectron spectroscopy (XPS; K-ALPHA, USA).

2.3 Cell viability

Cytotoxicity analysis was performed using a Cell Counting Kit-8 (CCK-8). Briefly, rat bone marrow mesenchymal stem cells (rBMSCs) were extracted from two-week-old Sprague–Dawley (SD) rats. Then, the isolated rBMSCs were plated in a 96-well microplate at a density of 5×10^3

per well. The cells were cultured in a-MEM with 10% FBS and 1% penicillin/streptomycin solution. After 24 h, the medium was replaced with conditioned mediums containing 0, 0.1, 1, 10, and 100 $\mu\text{g}/\text{mL}$ RGO@PDA, respectively. At the end of three intervals (1, 3, and 5 days), the appropriate amount of CCK-8 solution (Sigma-Aldrich, USA) was added to the medium. After 1 h, the optical density (OD) value of each well was recorded using a microplate reader (Varioskan LUX, USA) at 450 nm wavelength. Besides, the biocompatibility of RGO@PDA was also measured using a calcein AM/pi kit (Bioscience, China). First, the rBMSCs were plated in a 24-well microplate at a density of 2×10^4 per well. After 24 h, the medium was replaced with conditioned mediums containing different concentrations of RGO@PDA. After 1, 3, and 5 days, 500 μl a-MEM with the calcein AM and Propidium Iodide replaced the old medium. After incubating for 15 min, each well was observed by a fluorescence Microscope (Olympus, Japan).

2.4 ALP and ARS assay

Alkaline phosphatase assay kit (Beyotime, China) was used for ALP assay, and OD values were measured using a microplate reader at 405 nm. As well, NBT/BCIP staining kit (Beyotime, China) was used for ALP staining on day 7. Furthermore, alizarin red S (ARS) assay was performed on day 21. Briefly, rBMSCs were fixed for 30 min with 1 mL 4% neutral formaldehyde solution and then were washed with PBS. Then, 1 mL 1% ARS (Beyotime, China) was added to each well for 5 min. Finally, the plate was washed three times with PBS. To quantify the calcification, 10% CPC was used to desorb calcium ions, and OD values were measured using a microplate reader at 540 nm.

2.5 Intracellular ROS scavenging

The ROS scavenging assay was performed using a ROS assay kit (Beyotime, Shanghai, China). RAW264.7 cells (obtained from the West China Hospital of Stomatology, Sichuan University) were cultured in DMEM with 10% FBS and 1% penicillin/streptomycin solution and plated in 24-well plates (10^5 /well). After 12 h, the mediums were replaced with GO and RGO@PDA for 4 h. Then, cells were washed with PBS, and Rosup (150 mg/mL) was added in the medium for 30 min. To determine the ROS, the cell mediums were replaced with 2',7' - dichlorofluorescein diacetate (DCFH-DA), followed by incubation for 20 min at 37 °C and protected from light. Fluorescence microscopy images were recorded on a Leica imaging system. For the quantitative results, cells were detected using the Attune NxT Flow Cytometer.

Table 1 Primer sequences

Gene	Forward sequence	Reverse sequence
ALP	GGATCAAAGCAGCATCTTACCAG	GCTTTCCCATCTTCCGACACT
Runx2	CAGACCAGCAGCACTCCATA	GCTTCCATCAGCGTCAACAC
OCN	GAGGACCCTCTCTCTGCTCA	GGTAGCGCCGGAGTCTATT
COL1A1	AGAGGCATAAAGGGTCATCGTG	AGACCGTTGAGTCCATCTTTGC
IL-6	TTCACAAGTCGGAGGCTTA	CAAGTGCATCATCGTTGTTC
IL-1 β	TGGTGTGTGACGTTCCC	TGTCCATTGAGGTGGAGAG
TNF- α	CGCTGAGGTCAATCTGC	GGCTGGGTAGAGAATGGA
iNOS	ACGCTTCACTTCCAATGCAAC	CAGCCTCATGGTAAACACGTT
GAPDH	GACCCCTTCATTGACCTCAAC	CTTCTCCATGGTGGTGAAGA

2.6 RNA isolation and gene expression evaluation (real-time PCR)

RT-qPCR was used to evaluate the expression level of specific genes associated with osteogenesis and inflammation. After certain incubation times, RNA was extracted using the TRIzol reagent (Invitrogen, USA). Then, the cDNA was synthesized using the PrimeScript RT Reagent Kit. Subsequent RT-qPCR analysis was performed with the SYBR Premix Ex Taq II (Takara, Japan). The expression of mRNAs was normalized to the housekeeping gene GAPDH. Table 1 presents the primer sequences used in this study.

2.7 Western blot

The proteins were tested by Western blot (WB). Proteins were extracted using RIPA buffer (Beyotime, China) and measured using the BCA Protein Assay Kit (Beyotime, China). Equal quantities of protein samples were resolved by 10% sodium dodecyl sulfate-polyacrylamide gel electrophoresis (SDS-PAGE), transferred to poly (vinylidene fluoride) membranes (Millipore, USA), and blocked with 5% bovine serum albumin (BSA) for 1 h at room temperature. ALP (1:500, ET1601-21, Huabio, Hangzhou, China), Runx2 (1:500, ET1612-47, Huabio, Hangzhou, China), and GAPDH (1:10000; ER1706-83, Huabio, Hangzhou, China) antibodies were applied overnight at 4 °C. Following that, the blots were incubated with secondary antibodies at room temperature for 1 h. Images were observed by using the enhanced chemiluminescence (ECL) and the ChemiDocTM Imaging System (Bio-Rad, California, USA).

2.8 In vivo establishment of rat periodontitis

Twelve 8-week-old male Sprague-Dawley (SD) rats were obtained from the West China Hospital of Stomatology, Sichuan University. All surgical procedures were performed under general anesthesia induced by intraperitoneal

injection of 1% pentobarbital. Periodontitis was induced as previously described. Briefly, 0.2 mm diameter steel wire was tied around the maxillary second molar and inserted into the gingival sulcus for 3 consecutive weeks to prepare for treatment. Additionally, LPS was applied every 3 days in the gingival sulcus of the maxillary second molars. Then, GO and RGO@PDA were injected in the gingival sulcus every other day for 4-week treatment. Healthy rats without ligature and treatment were recognized as control group while rats with ligature but without treatment were recognized as periodontitis group.

2.9 Micro-CT analysis

The harvested maxillae were scanned by the micro-CT 50 system (SCANCO Medical, Switzerland; 70 kV, 200 mA, 10 μ m resolution). Three-dimensional (3D) images of the samples were reconstructed and segmented using the micro-CT system software. The distance of linear alveolar bone loss (ABL) was measured from the cemento-enamel junctions (CEJ) to alveolar bone crest (ABC) using Image J software (National Institutes of Health, Bethesda, MS, USA). Besides, bone-related parameter analysis was conducted by choosing the inter-radicular region of the distobuccal root of the M1 and the mesiobuccal root of the M2 as the region of interest (ROI), avoiding roots and other structures. A 60-slice volume was constructed in each sample. The bone volume/tissue volume ratio (BV/TV), trabecular thickness (Tb. Th.), and trabecular separation (Tb. Sp.) of the ROI were measured using SCANCO Evaluation software.

2.10 Histological staining, Masson's trichrome staining, and TRAP staining

Briefly, the major internal organs (heart, liver, spleen, lungs and kidneys) and maxillary tissue samples were soaked in 4% neutral buffered formalin, decalcified with EDTA, embedded in paraffin, and sectioned at a thickness of 5 μ m for hematoxylin-eosin (H&E), Masson's

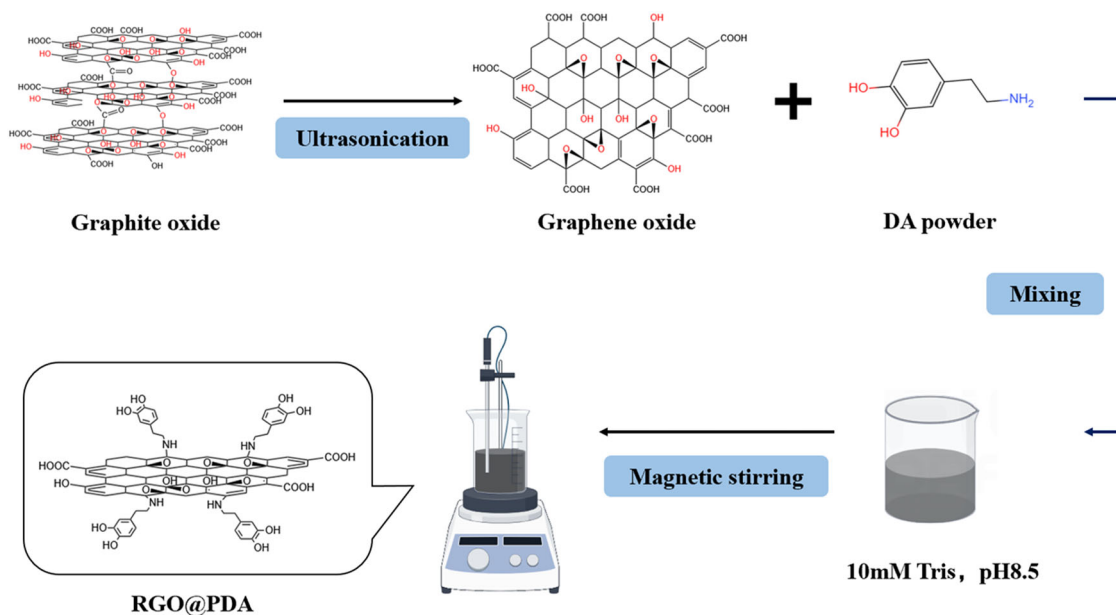


Fig. 1 Schematic illustration of the preparation of the RGO@PDA

trichrome and tartrate resistant acid phosphatase (TRAP) staining.

2.11 Immunohistochemical analysis

For IHC analysis, antibodies of TNF- α and Runx2 were used for overnight incubation at 4 °C with the sections. The integrated OD (IOD) and the area of positive expression were analyzed by the Image J software. The mean intensity was calculated with the following formula: Intensity = IOD/Area.

2.12 Statistical Analysis

This study's data were expressed as the mean \pm standard deviation calculated from three independent experiments. All results were analyzed by a one-way analysis of variance (ANOVA) accompanied by Tukey's post hoc test. Differences were assumed to be statistically significant when $P < 0.05$. The SPSS software package (Chicago, IL, USA) was used to analyze the data.

3 Results

3.1 Synthesis of RGO@PDA

RGO@PDA was synthesized by stirring the mixed solution (Fig. 1). Specifically, GO was partly reduced into RGO by DA, and then DA spontaneously polymerized and self-

assembled on the RGO surface, resulting in the final RGO@PDA.

3.2 The water dispersibility of RGO@PDA

As seen in Fig. 2A, after magnetically stirring for 12 h at room temperature, the yellow-brown GO dispersion turned dark black. The change of color was caused by the reduction of GO. The results of water dispersion showed that after 30 min, RGO-PDA-1 and RGO-PDA-2 were still dispersed in deionized water, while RGO-PDA-5 and RGO-PDA-10 were observed with aggregation and precipitation (Fig. 2B).

3.3 FTIR spectroscopy of RGO@PDA

As shown in Fig. 2C, GO showed four typical bands at 1719, 1618, 1114, and 1046 cm^{-1} , which were attributed to the C=O carboxyl stretching, aromatic C=C stretching, asymmetric and symmetric C-O stretching, respectively. In contrast, RGO-PDA showed a characteristic band at 3230 cm^{-1} , which corresponded to the N-H bond of PDA. Besides, the bands at 1500 and 1286 cm^{-1} were attributed to the stretching vibration of aromatic N-H and C-H. The appearance of these characteristic bands affirmed that PDA was self-polymerized onto the surface of GO. In addition, due to excessive content of PDA, the bands corresponding to C-N and N-H stretching vibrations became stronger in the RGO-PDA-5 and RGO-PDA-10 groups while the peaks of C=O were reduced distinctly.

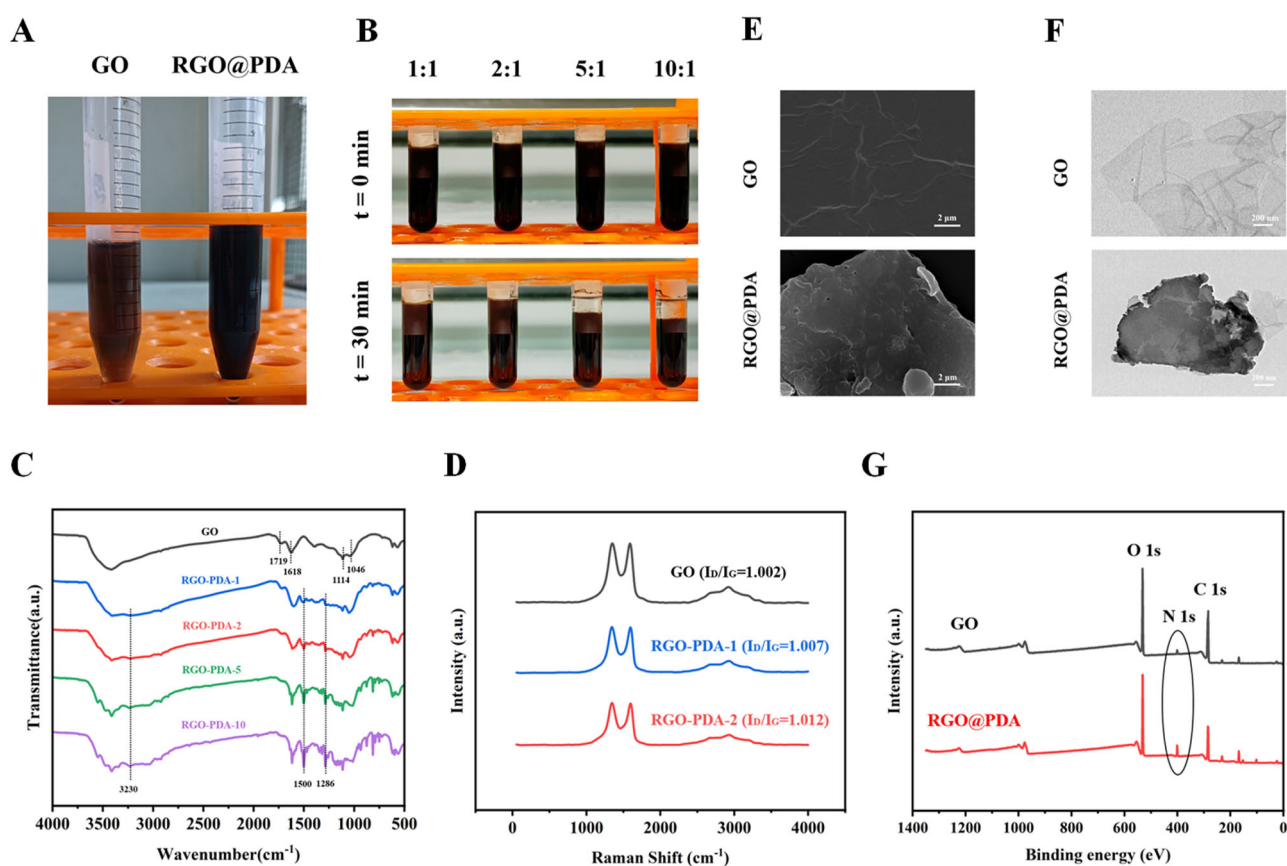


Fig. 2 Characterization of RGO@PDA. **A** Photographs of GO and RGO@PDA. **B** Digital images of RGO@PDA with different DA/GO ratios dispersed in deionized water after 30 min. **C** FTIR spectra and

D Raman spectra of GO and RGO@PDA with different DA/GO ratios. **E** SEM and **F** TEM images of GO and RGO@PDA. **G** XPS spectra of GO and RGO@PDA

3.4 Raman spectroscopy of RGO@PDA

As seen in Fig. 2D, all samples showed two distinct absorption peaks around 1350 and 1580 cm^{-1} , which were the D band formed by the vibration of defect-induced sp^3 carbon atoms and the G band representing the sp^2 carbon atoms in graphene, respectively. The intensity ratio of the D and G bands (I_D/I_G) is used to determine the degree of defects for graphene-based materials. Compared with GO, the I_D/I_G ratios of RGO-PDA groups were slightly increased. This may be due to the π - π conjugation effect between DA and GO, which increased the surface disorder of GO and lead to carbon defects. However, the I_D/I_G ratios among GO, RGO@PDA-1, and RGO@PDA-2 are still very close, indicating that the basic structure and properties of graphene sheets are preserved.

3.5 SEM and TEM of RGO@PDA

Figure 2E shows the SEM images of both materials, respectively. GO showed a closely packed lamellar structure and a flaky texture. The RGO@PDA contained several

layers of aggregated and square-shaped crumpled sheets closely associated with each other to form a continuous conducting network. Figure 2F shows the TEM images of both materials, respectively. GO had a transparent thin sheet structure, which seemed like a wrinkled veil. On the contrary, RGO@PDA exhibited dense and opaque surface. Compared to GO, the opacity of RGO@PDA was changed, and the edges of RGO@PDA were much fuzzy, suggesting the coating of PDA layer on GO sheet.

3.6 XPS spectroscopy of RGO@PDA

As seen in Fig. 2G, GO and RGO@PDA both exhibited peaks at 285 and 531 eV, attributing to C1s and O1s, respectively, while RGO@PDA clearly showed N1s peaks with a binding energy of 400 eV, which indicated that DA was successfully modified on the surface of GO surface.

3.7 Cell viability assay and hemocompatibility property of RGO@PDA

As shown in Fig. 3A, on the first day, the cell viability of rBMSCs fell sharply when the concentration of

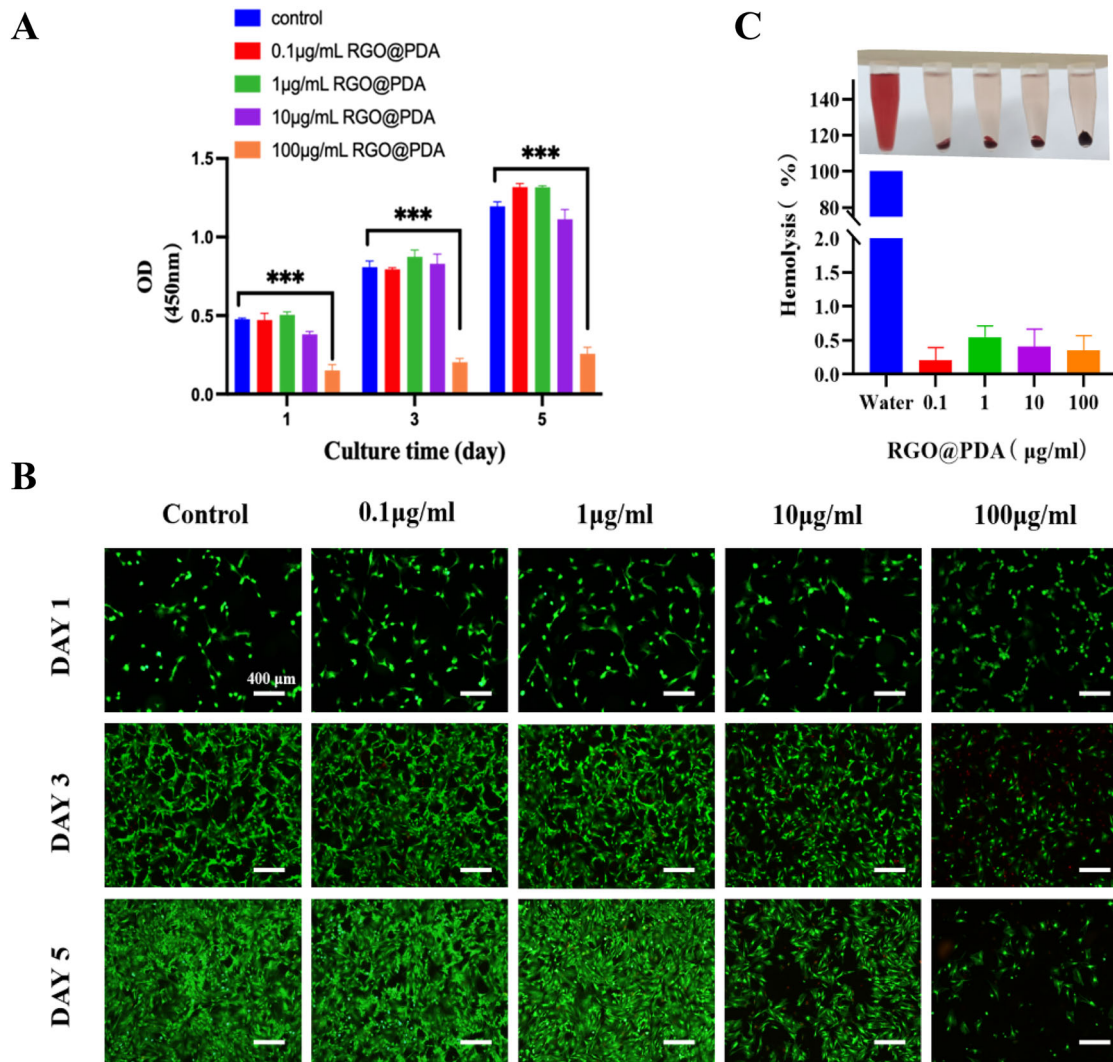


Fig. 3 Biocompatibility of RGO@PDA. **A** CCK-8 assay of rBMSCs treated with RGO@PDA. Cells without RGO@PDA served as a control. **B** Live/Dead staining of rBMSCs. Green fluorescence: Calcein AM

represented live cells; red fluorescence: PI represented dead cells. Scale bar: 400 µm. **C** Hemolysis assay of RGO@PDA. All data are presented as mean \pm SD ($n = 3$). Statistical analysis: * $P < 0.05$; ** $P < 0.01$; *** $P < 0.001$

RGO@PDA was 100 µg/ml. On the fifth day, there was an obvious difference in OD values between the control group and RGO@PDA group with a concentration of 10 µg/ml. RGO@PDA maintained remarkable biocompatibility during the five days when the final concentration was ≤ 1 µg/ml. The merged fluorescent microscopy images (Fig. 3B) showed that rBMSCs exhibited strong green fluorescence when the concentration of RGO@PDA was ≤ 1 µg/ml at every timepoint, suggesting that cells were viable under the concentration. The results of CCK-8 and fluorescent microscopy indicated RGO@PDA was biocompatible when the concentration was ≤ 1 µg/ml. RGO@PDA with all concentrations showed a low hemolysis rate, suggesting

RGO@PDA could be in contact with blood for a long period of time. (Fig. 3C).

3.8 The optimal concentration of RGO@PDA for ALP activity of rBMSCs

As seen in Fig. S1, compared with the control group, which was without RGO@PDA, rBMSCs cultured with 0.1 and 1 µg/ml RGO@PDA demonstrated significantly increased alkaline phosphatase (ALP) activity. However, with the further increase of the concentration, ALP activity decreased instead, which might be the fact that high concentration of RGO@PDA inhibited the growth of rBMSCs. Consequently, we chose 1 µg/ml RGO@PDA for subsequent experiments.

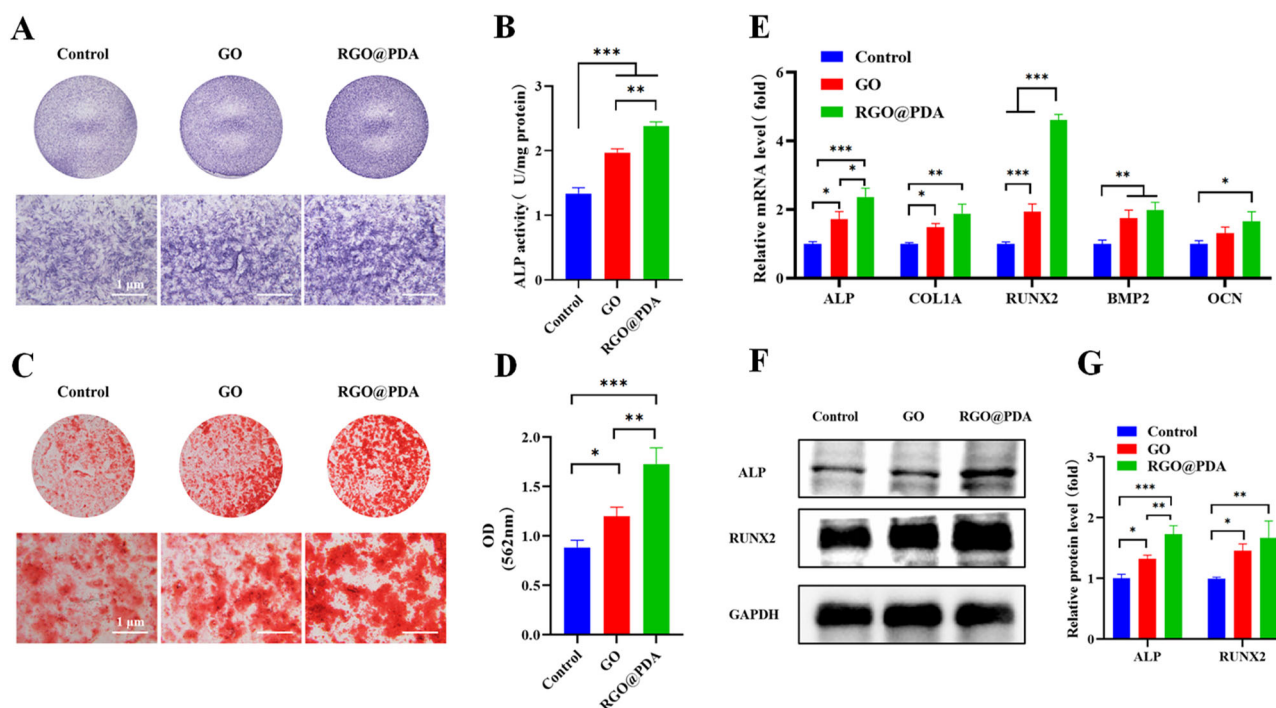


Fig. 4 RGO@PDA induced osteogenic differentiation of rBMSCs. **A, B** ALP staining and ALP activity quantitative analyzes of rBMSCs after 7 days cultured with GO or RGO@PDA. Scale bar: 1 μ m. **C, D** ARS staining and quantitative analyzes of rBMSCs after 21 days

cultured with GO or RGO@PDA. (**E–G**) Relative mRNA expression and protein level of osteogenic genes. All data are presented as mean \pm SD ($n = 3$). Statistical analysis: NS non-significant; * $P < 0.05$; ** $P < 0.01$; *** $P < 0.001$

3.9 Effect of RGO@PDA on the ALP staining and ARS staining of rBMSCs

The results of ALP staining and activity assay showed that both RGO@PDA and GO could act synergistically with osteogenesis-inducing medium to promote the expression of ALP in rBMSCs, while the area of the blue NBT-formazan (which is catalyzed by ALP) in the RGO@PDA group was larger than that of the GO group at day 7 (Fig. 4A, B).

The ARS staining results are shown in Fig. 4C, D, a large area of deep red calcium nodule deposits was seen in the RGO@PDA group, while the calcium nodule deposits of the GO group were significantly smaller. The control group had only a few calcium nodule deposits. The results of ARS semi-quantitative analysis were consistent with those of ARS staining.

3.10 The expression of osteogenic-related genes and proteins of rBMSCs

Compared with the other two groups, all kinds of osteogenic genes were significantly up-regulated in the RGO@PDA group (Fig. 4E). There was no significant difference in the gene expression level of OCN between RGO@PDA group and GO group. Although GO could also promote the osteogenic differentiation of rBMSCs, the promoting effect of RGO@PDA on the osteogenic

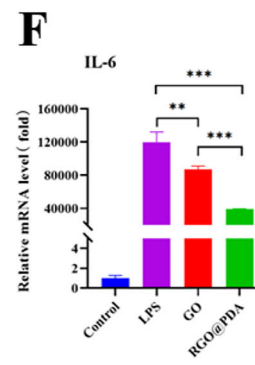
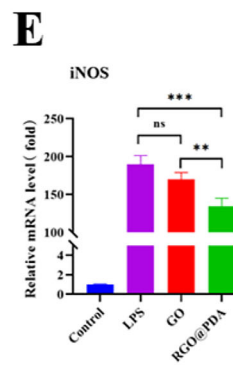
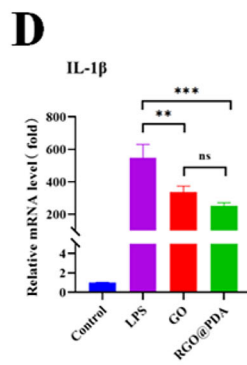
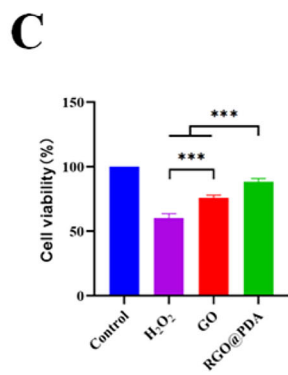
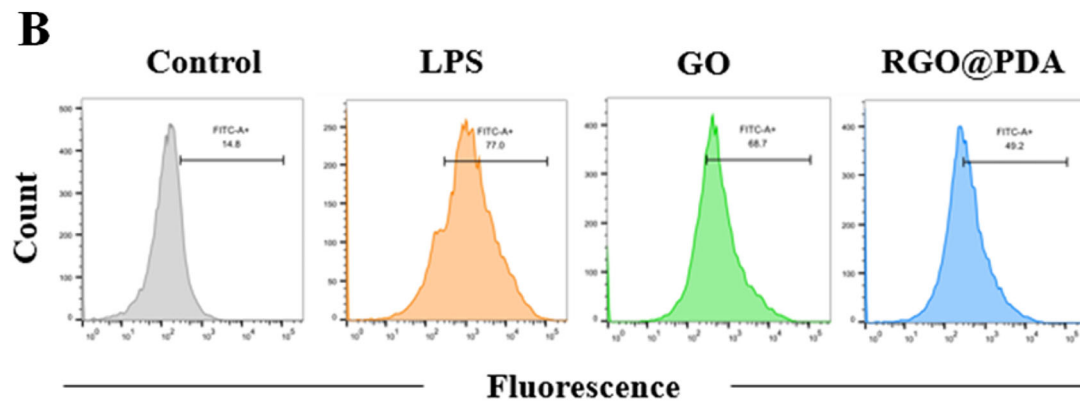
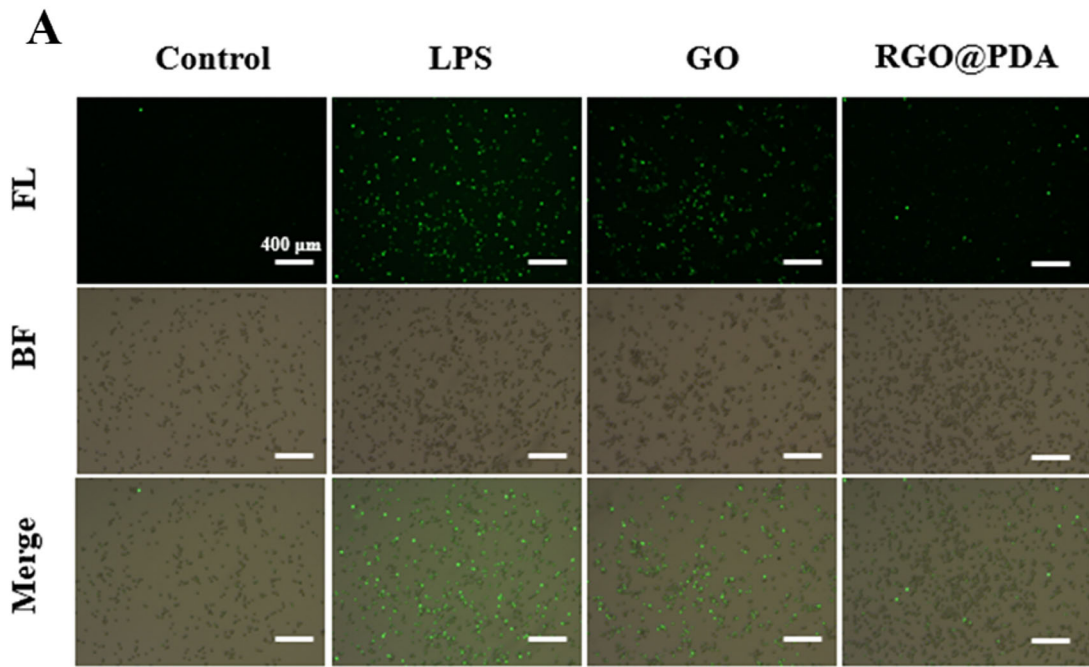
differentiation of rBMSCs was more remarkable. The results of western blot showed that the protein expressions of ALP and RUNX2 in rBMSCs treated with RGO@PDA were increased significantly compared with the control group (Fig. 4F, G).

3.11 Intracellular ROS scavenging and anti-inflammatory effects of RGO@PDA

After being stimulated by Rosup, obvious green fluorescence could be observed in the positive control group, which implied the successful establishment of the oxidative stress model (Fig. 5A). Compared to the positive control group, RGO@PDA effectively reduced ROS with the lowest fluorescence intensity. As shown in Fig. 5B, the ROS positivity of the GO in RAW264.7 was 68.7% while the ROS positivity was reduced to 49.2% in the RGO@PDA group.

The results of the CCK-8 test verified the effectiveness of RGO@PDA in preventing cell damage from oxidative stress. After being stimulated by H_2O_2 , the cell viability decreased to 60.28% (Fig. 5C). In contrast, the cell viability was recovered to 75.95% by GO and to 88.61% by RGO@PDA.

The RT-qPCR results showed that RGO@PDA significantly downregulated the expression of inflammatory factors after lipopolysaccharide (LPS) stimulation.



◀ **Fig. 5** ROS scavenging and anti-inflammatory effects of RGO@PDA. **A** (Fluorescence imaging of intracellular ROS scavenging capacity. Green fluorescence: DCFH-DA labels the intracellular ROS. Scale bar: 400 μ m. **B** Flow cytometry of the intracellular ROS levels of RAW264.7 cells treated with GO or RGO@PDA. A negative control consists of cells without Rosup stimulation and without treatment, while a positive control contains cells with Rosup stimulation but without treatment. **C** Cytoprotective properties under oxidative stress (750 μ M H₂O₂) examined by CCK-8 assay. All data are presented as mean \pm SD (n = 3). **D** The qPCR results of inflammation-related cytokines of Raw264.7 cells pretreated with GO or RGO@PDA. All data are presented as mean \pm SD (n = 3). Statistical analysis: NS non-significant; * P < 0.05; ** P < 0.01; *** P < 0.001

Although both RGO@PDA and GO reduced the expression of the inflammatory factors, RGO@PDA inhibited the mRNA expression of IL-6, TNF- α , and iNOS more significantly than GO (Fig. 5D–F).

3.12 Micro-CT analysis

The rat periodontitis models were established by orthodontic wire ligation and LPS, then we injected the rats with RGO@PDA for therapy (Fig. 6A, B).

3D Micro-CT reconstruction was performed to detect the periodontal destruction at 4 weeks post-surgery. The amount of bone loss was represented as the linear distance between the distal cemento-enamel junction (CEJ) of the second molar and the apex of the alveolar ridge (ABC). As shown in Fig. 6C, orthodontic wire ligation successfully induced periodontitis in rats and resulted in considerable bone loss, with the RGO@PDA group showing greater difference in the CEJ-ABC distance than the periodontitis group (Fig. 6D). The quantitative results of BV/TV ratio, trabecula separation (Tb.Sp.) trabecula thickness (Tb.Th.) and indicated that RGO@PDA significantly suppressed bone osteolysis and improved bone reconstruction (Fig. 6E–G).

3.13 H&E staining, Masson's trichrome staining and TRAP staining

H&E staining and Masson's trichrome staining were seen in Fig. 7A, B. The periodontitis group experienced a thickened epithelium layer, increased inflammatory cell infiltration (black triangle in Fig. 7A), degraded fibers, and alveolar bone loss. In contrast, although the GO group showed confined inflammatory lesions and fewer inflammatory cells, the RGO@PDA group showed the least inflammatory infiltration and most reduced height of alveolar bone with more orderly-arranged periodontal fibers tightly adhering to the bone surface (Fig. 7B), indicating an obvious therapeutic effect in periodontitis.

TRAP staining was shown in Fig. 7C. A decreased number of TRAP-positive cells (black arrows in Fig. 7C)

along the alveolar bone surface were observed in RGO@PDA group, demonstrating an obvious inhibition of osteoclast activity.

In addition, we collected the hearts, livers, spleens, lungs, and kidneys of rats to evaluate the long-term toxicity of RGO@PDA via local subgingival administration on these organs by H&E staining (Fig. S2). The results showed no histological differences between the healthy and RGO@PDA groups.

3.14 Immunohistochemical analysis

The results of immunohistochemical analysis showed that the periodontitis group possessed a large area of deep staining for the inflammatory factor TNF- α while the stained area of the RGO@PDA group seemed confined and light (Fig. 8A), which was in accordance with the quantitative results (Fig. 8B). Moreover, compared to the periodontitis and GO groups, the RGO@PDA group exhibited the highest immunostaining of Runx2 (Fig. 8C, D).

4 Discussion

The progression of periodontitis is a dynamic and intricate process involving multiple mechanisms, including oxidative stress, inflammatory responses, and immune regulation. In this study, we successfully synthesized RGO@PDA using a straightforward and efficient magnetic stirring method. During this process, GO was reduced to RGO by the catechol moieties of DA, and then DA spontaneously polymerized and self-assembled into PDA on the surface of RGO. As the PDA clusters continued to grow and aggregate, the final dark black RGO@PDA composite was obtained [37].

To determine the optimal DA/GO ratio for synthesizing RGO@PDA, we evaluated the water dispersibility and physicochemical properties of RGO@PDA prepared at different DA/GO ratios (1:1, 2:1, 5:1, and 10:1). The results revealed that RGO@PDA-2, compared to RGO@PDA-5 and RGO@PDA-10, retained the fundamental structure and properties of GO while exhibiting excellent water dispersibility. Furthermore, RGO@PDA-2 incorporated more DA than RGO@PDA-1, enhancing the synergistic effects of DA and GO. These findings align with the research of Jia et al. [38], which also confirmed that a DA/GO ratio of 2:1 yields RGO@PDA with superior physicochemical properties and biological functionality. Thus, a DA/GO ratio of 2:1 was identified as the optimal condition for synthesizing RGO@PDA.

Therefore, a DA/GO ratio of 2:1 was selected for all subsequent experiments (unless otherwise specified, RGO@PDA refers to the material synthesized with a DA/

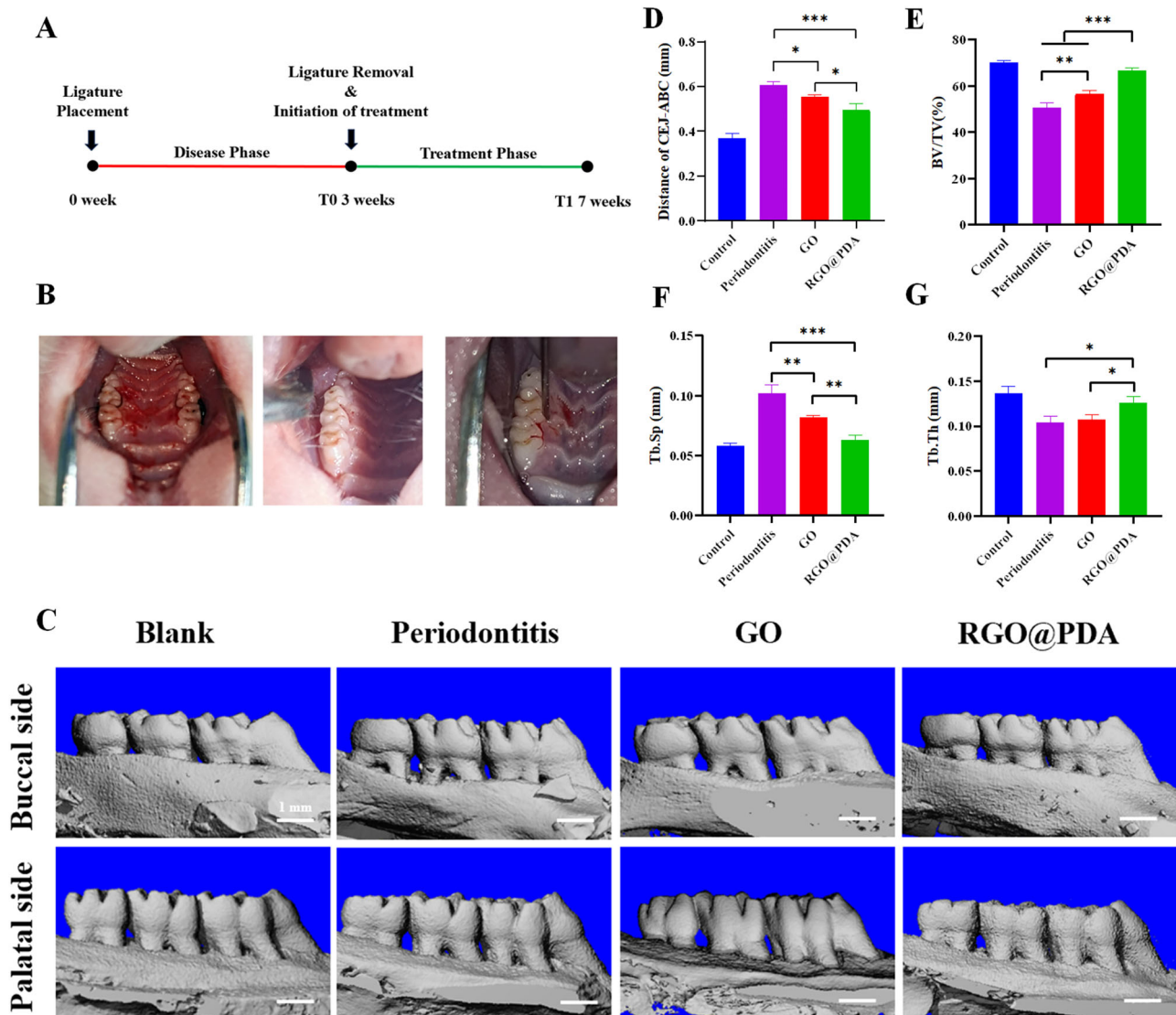


Fig. 6 In vivo periodontitis model establishment and MicroCT results. **A** Schematic illustration of the timeline began with 3 weeks of experimental periodontitis, followed 4-week local administration of RGO@PDA in rats. **B** Orthodontic ligature wire (diameter = 0.2 mm) was inserted around second molar and treatment of periodontal tissues

around the ligature side of maxillary molars, 100 μ L per site. **C** MicroCT results. **D** CEJ-ABC distance. **(E)** BV/TV, **(F)** Tb.sp., and **G** Tb.th. calculated by micro-CT images. All data are presented as mean \pm SD ($n = 3$). Statistical analysis: NS non-significant; * $P < 0.05$; ** $P < 0.01$; *** $P < 0.001$

GO ratio of 2:1). The successful coating of PDA on RGO was confirmed by FTIR spectroscopy. As shown in Fig. 2C, GO exhibited characteristic peaks at 1719 cm^{-1} (C=O stretching of carboxyl groups), 1618 cm^{-1} (C=C skeletal vibration of sp^2 carbon domains), 1114 cm^{-1} (C-O-C asymmetric stretching of epoxide groups), and 1046 cm^{-1} (C-OH stretching of hydroxyl groups). In contrast, RGO@PDA showed a broad peak at 3230 cm^{-1} , corresponding to N-H stretching vibrations from PDA, along with new peaks at 1500 cm^{-1} (attributed to C=N stretching of quinone-imine structures in PDA) and 1286 cm^{-1} (C-N-C stretching in PDA backbone). The disappearance of GO's C=O (1719 cm^{-1}) and C-O-C (1114 cm^{-1}) peaks, coupled with the emergence of PDA-specific signals,

confirmed the reduction of GO to RGO and the self-polymerization of PDA on its surface [39, 40]. XPS analysis (Fig. 2G) confirmed the presence of nitrogen in RGO@PDA, with a prominent N1s peak centered at 400 eV. The N1s peak may have three components: 399.3 eV (amine groups, $-\text{NH}/-\text{NH}_2$), 400.5 eV (protonated amines, $-\text{NH}^+=$), and 401.8 eV (quinone-imine groups, $-\text{N}=\text{}$), consistent with the chemical structure of PDA [41, 42]. The absence of nitrogen signals in pristine GO further validates the successful coating of PDA on RGO.

The excellent water dispersibility of RGO@PDA was evidenced by its homogeneous distribution in PBS with no visible sedimentation over 30 min (Fig. 2B), indicating

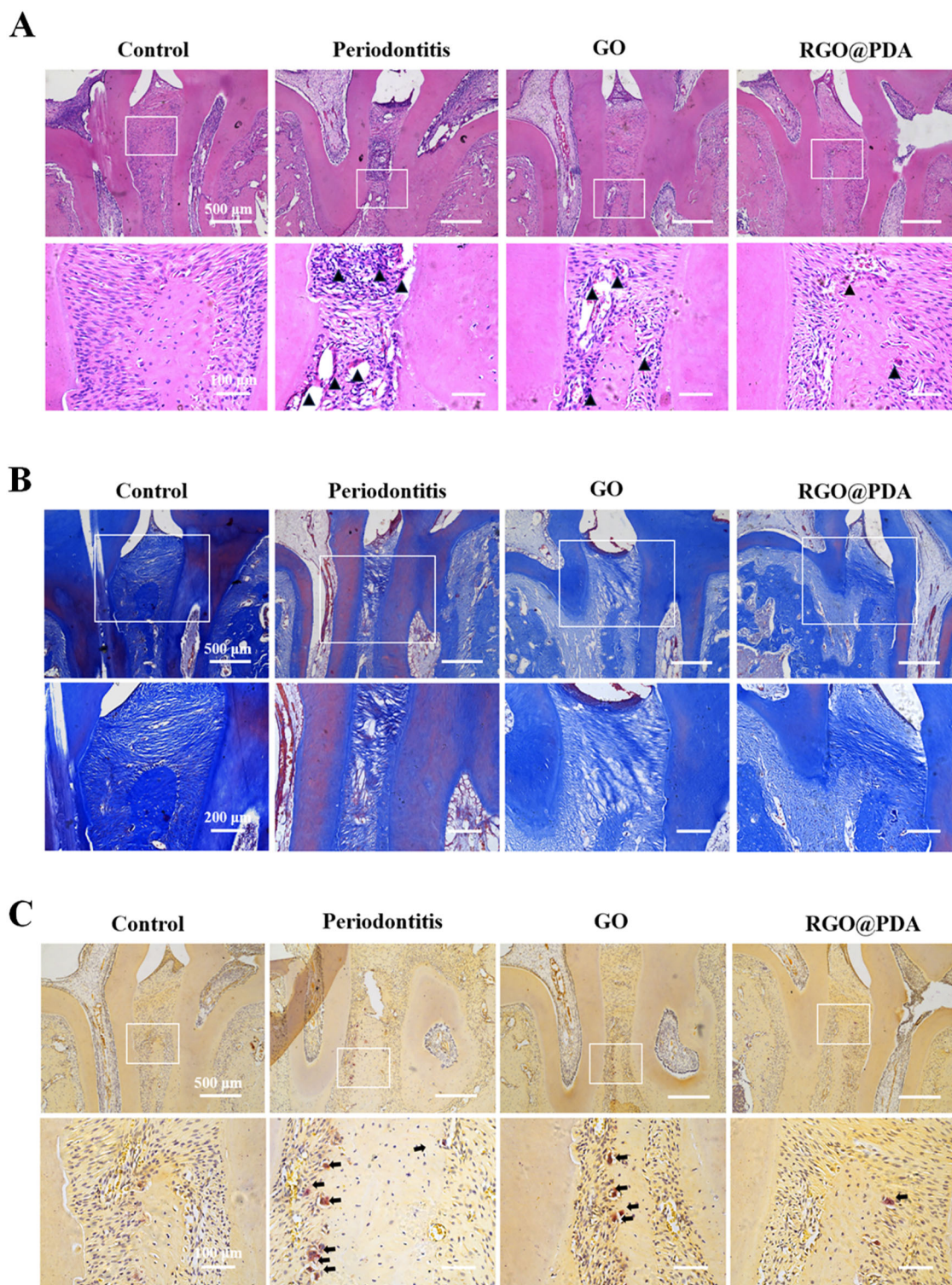


Fig. 7 Histological staining of maxillary alveolar bone. **A** H&E staining. The black triangles indicate the immune cells. **B** Masson staining. **C** Tartrate-resistant acid phosphatase (TRAP) staining. The black arrows indicate TRAP-positive (stained red) cells

excellent stability in physiological environments. SEM and TEM images further confirmed the uniform dispersion of RGO@PDA as individual nanosheets (Fig. 2E), with PDA coating effectively smoothing the sharp edges of RGO (Fig. 2F). This morphological feature minimizes the risk of

cellular membrane damage caused by aggregated or sharp-edged particles, thereby supporting its biocompatibility [43, 44]. Although SEM and TEM images were obtained in the dry state, prior studies have demonstrated that such structural characteristics strongly correlate with dispersion

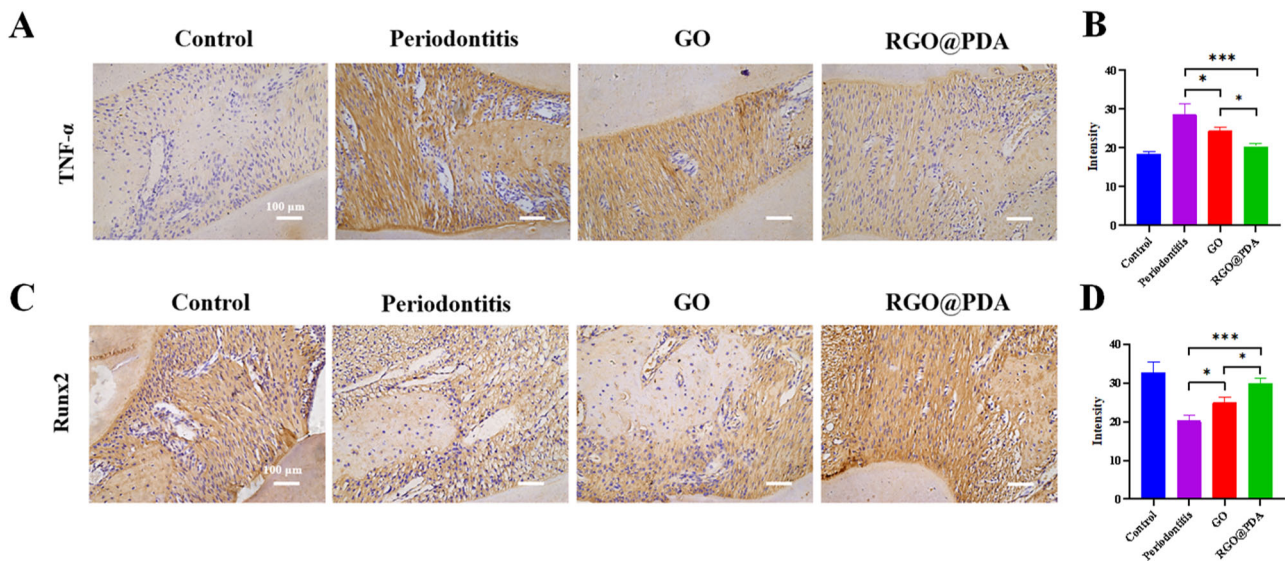


Fig. 8 Representative images of immunohistochemical staining of TNF- α (A) and corresponding quantitative results (B). Representative images of immunohistochemical staining of RUNX2 (C) and

corresponding quantitative results (D). All data are presented as mean \pm SD ($n = 3$). Statistical analysis: NS non-significant; * $P < 0.05$; ** $P < 0.01$; *** $P < 0.001$

behavior in hydrated conditions [45]. Overall, RGO@PDA stands out for its simple composition and straightforward preparation process, which eliminates the need for additional chemical cross-linking agents. Its excellent water dispersibility and physicochemical properties further underscore its potential as a highly promising biomaterial for diverse applications.

Then, we evaluated the cytotoxicity of RGO@PDA. The differentiation potential of mesenchymal stem cells (MSCs) has garnered significant global attention, with prior researches indicating their promise as an effective approach for periodontal regenerative therapy [46, 47]. Therefore, characterizing and modifying biomaterials that can influence the osteogenic differentiation of MSCs holds great significance for bone tissue regeneration. Given the ease of obtaining rat bone marrow mesenchymal stem cells (rBMSCs) and their similarity to human mesenchymal stem cells (hMSCs), we selected rBMSCs for in vitro experiments. Using CCK-8 assays and fluorescence microscopy, we found that RGO@PDA exhibited biocompatibility at concentrations $\leq 1 \mu\text{g/mL}$. However, RGO@PDA demonstrated dose-dependent cytotoxicity, which is attributed to the graphene oxide nanosheets. Numerous studies have reported the cytotoxic effects of graphene oxide at high concentrations [48–51]. PDA-coating promoted cell adhesion and proliferation on substrates as compared to the pristine substrates [52], so it's reasonable to assume that the coating of PDA could enhance the biocompatibility of GO. These findings highlight the importance of optimizing RGO@PDA concentrations to balance biocompatibility and therapeutic efficacy.

Next, we compared the osteogenic differentiation between GO and RGO@PDA. The expression and activity of ALP are closely associated with the osteogenic differentiation of BMSCs and serve as a crucial component in the early formation of bone tissue [53]. So we identified the optimal concentration of RGO@PDA that most favorably promotes the osteogenic differentiation of rBMSCs through ALP activity assays. This optimal concentration, determined to be $1 \mu\text{g/mL}$, was subsequently used for both RGO@PDA and GO in the following experiments.

Subsequently, ALP staining and activity assays revealed that both RGO@PDA and GO could synergize with osteogenic induction medium to enhance ALP expression in rBMSCs. Notably, on day 7, RGO@PDA demonstrated a superior ability to promote ALP formation compared to the GO group and the control group, indicating that RGO@PDA actively participates in the early osteogenic differentiation of rBMSCs. In the later stages of osteogenesis, cell mineralization occurs, and calcium nodules begin to deposit [54]. As a significant marker of mature osteoblast differentiation, calcium nodules not only represent the primary morphological feature of osteoblasts performing their function but also reflect the activity and functional state of osteoblasts. ARS specifically reacts with calcium nodules to form a vivid orange-red or deep red complex, commonly used to indicate the formation and distribution of calcium nodules. ARS staining and quantitative analysis showed that, compared to the control group, the RGO@PDA group exhibited larger, darker, and more numerous calcium nodules, underscoring the role of RGO@PDA in promoting late-stage osteogenesis in rBMSCs.

To further evaluate the osteo-inductive effects of RGO@PDA at gene level, we examined the expression of osteogenic-related genes by RT-qPCR. ALP, COL1A1, RUNX2, BMP2, and OCN all act as regulatory factors involved in bone formation [55]. Compared with the other two groups, all kinds of osteogenic genes were significantly up-regulated in the RGO@PDA group. This result further indicated that RGO@PDA could promote osteogenic differentiation of rBMSCs. It was noteworthy that there was no statistically significant difference in the gene expression level of OCN between RGO@PDA group and GO group. The reason for this might be that as early as day 7, rBMSCs probably had not yet entered the late stage of osteogenic differentiation, and OCN was not yet fully expressed. In addition, we also explored the effect of RGO@PDA on osteogenic differentiation of rBMSCs at protein level, and the results showed the same trend as gene levels.

Many studies have shown elevated levels of oxidative stress markers in periodontitis patients compared to healthy patients, which emphasized the link between oxidative stress and periodontitis [56, 57]. It has been reported that GO exhibits significant antioxidant properties by scavenging hydroxyl and superoxide radicals, thereby protecting various biological target molecules from oxidation. The antioxidant performance of GO is primarily associated with the sp^2 carbon atoms on the graphene surface [58]. In addition, PDA can exert antioxidant capabilities through the catechol groups in its chemical structure, enabling it to scavenge free radicals under oxidative stress micro-environments [59]. Since RGO@PDA retains the sp^2 carbon atoms of GO and provides a platform for the self-polymerization of DA into PDA, it is reasonable to consider that RGO@PDA possesses certain antioxidant capabilities. Our experimental results confirmed that, compared to GO, RGO@PDA exhibited significant ROS scavenging ability, and the CCK-8 results demonstrated that RGO@PDA had a protective effect on RAW264.7 cells under oxidative stress conditions, which both proving the antioxidant capacity of RGO@PDA.

Apart from ROS, inflammatory factors secreted by macrophages are closely associated with the acute inflammatory response and tissue destruction [60]. During the active phase of periodontitis, there is a significant accumulation of inflammatory mediators such as IL-6 and TNF- α . These inflammatory mediators recruit more inflammatory cells, amplifying the inflammatory response and stimulating osteoclast formation, which leads to inflammation of periodontal soft tissues and alveolar bone resorption [61, 62]. Furthermore, various inflammatory factors in the inflammatory microenvironment, such as TNF- α and IL-1 β , have been proven to inhibit the osteogenic differentiation of stem cells [63]. Therefore, we detected the expression of the proinflammatory genes IL-1 β , IL-6, TNF- α , and iNOS by

RT-qPCR. The results showed that RGO@PDA inhibited the mRNA expression of IL-6, TNF- α , and iNOS more significantly than GO. Overall, these results provide new evidence for the ROS scavenging and anti-inflammatory effects of RGO@PDA.

To better determine the role of RGO@PDA in periodontitis, we established a rat periodontitis model by orthodontic wire ligation and LPS [64]. Then we injected the rats with RGO@PDA for therapy. Local drug injection in periodontal pocket is an effective way of drug intervention, which can increase the local drug concentration and is similar to the clinical treatment of periodontitis. This method is widely used in the establishment of rat periodontitis model [65]. 3D Micro-CT reconstruction was performed to detect the periodontal destruction at 4 weeks post-surgery. The results showed that the RGO@PDA group exhibited only a slight decrease in alveolar bone height, and the relevant parameters of bone microstructure showed significant improvement, alleviating alveolar bone resorption under inflammatory conditions of periodontitis. In terms of soft tissue inflammation, we conducted histological staining on the maxillary samples of rats to further evaluate the therapeutic effects of RGO@PDA on pathological changes in periodontal soft tissues. The results demonstrated that RGO@PDA not only inhibited the loss of periodontal hard tissues but also alleviated inflammation in periodontal soft tissues. These two effects interacted and mutually reinforced each other, ultimately leading to a favorable therapeutic outcome for periodontitis. In addition, immunohistochemical staining results revealed that RGO@PDA can effectively suppress the expression of the inflammatory factor TNF- α while promoting the expression of the osteogenic differentiation marker RUNX2. This further illustrated the dual role of RGO@PDA in both anti-inflammatory and osteogenic effects. In this study, the *in vivo* therapeutic effects of RGO@PDA were compared with those of GO, untreated periodontitis models, and healthy controls. The experimental design prioritized periodontal bone regeneration, with a focus on the composite's osteogenic performance. Building upon the well-documented osteogenic potential of GO and our *in vitro* findings demonstrating that PDA functionalization enhances graphene biocompatibility, we hypothesized that RGO@PDA would exhibit superior bone regenerative capacity compared to GO alone. This hypothesis was validated by *in vitro* experiments showing that RGO@PDA significantly enhanced osteogenic differentiation and mineralization relative to unmodified GO. While RGO-only and PDA-only groups were not included in the *in vivo* model, this design was based on the premise that the synergistic osteogenic and anti-inflammatory effects of RGO and PDA are critical for achieving functional bone regeneration. Previous studies have shown that standalone

RGO exhibits limited bioactivity due to aggregation tendencies [66, 67], while PDA alone lacks the structural support required for sustained drug delivery [68, 69]. Future studies will systematically compare RGO@PDA, RGO-only, and PDA-only treatments to dissect their individual contributions and validate potential synergies.

Although the current study did not experimentally validate the specific signaling pathways involved in RGO@PDA-mediated osteogenesis and anti-inflammatory effects, existing literature provides plausible mechanistic insights. Previous studies have shown that the osteogenesis-inductive ability of GO may be related to the Wnt/ β -catenin signaling pathway and MAPK/JNK signaling pathway. The Wnt/ β -catenin pathway is known to regulate osteoblast differentiation and bone formation, and graphene-based materials have been shown to activate this pathway via mechanical or chemical cues [49, 70]. Similarly, the MAPK/JNK pathway may mediate cellular responses to oxidative stress, potentially explaining RGO@PDA's dual role in promoting osteogenesis and scavenging ROS [71]. Additionally, the anti-inflammatory effects of RGO@PDA, as evidenced by reduced proinflammatory cytokine expression, may involve suppression of the NF- κ B pathway, a key regulator of inflammatory responses [72]. The main limitation of the present study is the lack of research into the osteo-inductive mechanism. Future studies will focus on systematically investigating these pathways through RNA sequencing and siRNA-mediated gene silencing to elucidate the molecular mechanisms underlying RGO@PDA's bioactivity.

In addition, we collected the hearts, livers, spleens, lungs, and kidneys of rats to evaluate the long-term toxicity of RGO@PDA via local subgingival administration on these organs by H&E staining. The results showed no histological differences between the healthy group and RGO@PDA groups. Combined with the results of *in vitro* biocompatibility studies on RGO@PDA, it can be found that low concentration of RGO@PDA not only showed excellent biocompatibility *in vitro*, but also had excellent biosafety *in vivo*. This finding provided a solid and reliable experimental basis for its application in clinical practice. Besides, it had been proved that GO not only showed degradability in water [73], but there were also possible degradation pathways in the human body. Recent studies have found that activated human neutrophil peroxidase (hMPO) can cause biodegradation of GO [74, 75]. Furthermore, Bao et al. [76] found that PDA nanoparticles were biodegradable through local gum injection of periodontitis mice, which may be due to the uptake, transport, and release of biological materials by macrophages. These results provided some evidence for the biodegradability of RGO@PDA. However, further studies are needed to explore the biodegradability pathway of RGO@PDA

in vivo to provide stronger support for the clinical application of RGO@PDA.

5 Conclusions

In this study, we demonstrated the anti-inflammatory and osteogenic potential of RGO@PDA both *in vitro* and *in vivo*. A simple and efficient method was developed to synthesize the biocompatible and water-dispersible RGO@PDA composite. *In vitro* experiments revealed that RGO@PDA not only promoted osteogenesis by enhancing ALP activity, mineralization, and the expression of osteogenic genes and proteins but also effectively scavenged ROS and suppressed proinflammatory factors, creating a favorable microenvironment for bone formation. *In vivo* studies further confirmed that RGO@PDA alleviated inflammation and enhanced alveolar bone repair. These findings highlight the potential of RGO@PDA for the treatment of periodontitis-induced bone defects and provide new insights into the dental applications of graphene-based materials.

Data availability

The datasets generated for and/or analyzed during the current study are available from the corresponding author upon reasonable request.

Supplementary information The online version contains supplementary material available at <https://doi.org/10.1007/s10856-025-06905-3>.

Acknowledgements This work was supported by Science and Technology Department of Sichuan Province (2022YFS0127).

Compliance with ethical standards

Conflict of interest The authors declare that they have no known competing financial interests or personal relationships that could have influenced the work reported in this paper.

Publisher's note Springer Nature remains neutral with regard to jurisdictional claims in published maps and institutional affiliations.

Open Access This article is licensed under a Creative Commons Attribution-NonCommercial-NoDerivatives 4.0 International License, which permits any non-commercial use, sharing, distribution and reproduction in any medium or format, as long as you give appropriate credit to the original author(s) and the source, provide a link to the Creative Commons licence, and indicate if you modified the licensed material. You do not have permission under this licence to share adapted material derived from this article or parts of it. The images or other third party material in this article are included in the article's Creative Commons licence, unless indicated otherwise in a credit line to the material. If material is not included in the article's Creative Commons licence and your intended use is not permitted by statutory regulation or exceeds the permitted use, you will need to obtain

permission directly from the copyright holder. To view a copy of this licence, visit <http://creativecommons.org/licenses/by-nc-nd/4.0/>.

References

1. Kassebaum NJ, Bernabé E, Dahiya M, Bhandari B, Murray CJ, Marcenes W. Global burden of severe periodontitis in 1990–2010: a systematic review and metaregression. *J. Dent. Res.* 2014;93:1045–53. <https://doi.org/10.1177/0022034514552491>.
2. Pihlstrom B, Michalowicz B, Johnson N. Periodontal diseases. *Lancet.* 2005;366:1809–20. [https://doi.org/10.1016/S0140-6736\(05\)67728-8](https://doi.org/10.1016/S0140-6736(05)67728-8).
3. Preshaw PM, Alba AL, Herrera D, Jepsen S, Konstantinidis A, Makrilakis K, et al. Periodontitis and diabetes: a two-way relationship. *Diabetologia.* 2012;55:21–31. <https://doi.org/10.1007/s00125-011-2342-y>.
4. Sanz M, Marco Del Castillo A, Jepsen S, Gonzalez-Juanatey JR, D'Aiuto F, Bouchard P, et al. Periodontitis and cardiovascular diseases: consensus report. *J. Clin. Periodontol.* 2020;47:268–88. <https://doi.org/10.1111/jcpe.13189>.
5. Ouyang Y, Liu J, Wen S, Xu Y, Zhang Z, Pi Y, et al. Association between chronic obstructive pulmonary disease and periodontitis: the common role of innate immune cells? *Cytokine.* 2022;158:155982 <https://doi.org/10.1016/j.cyto.2022.155982>.
6. Graziani F, Karapetsa D, Alonso B, Herrera D. Nonsurgical and surgical treatment of periodontitis: how many options for one disease? *Periodontology.* 2017;75:152–88. <https://doi.org/10.1111/prd.12201>.
7. Graziani F, Karapetsa D, Mardas N, Leow N, Donos N. Surgical treatment of the residual periodontal pocket. *Periodontology.* 2018;76:150–63. <https://doi.org/10.1111/prd.12156>.
8. Coello R, Charlett A, Wilson J, Ward V, Pearson A, Borriello P. Adverse impact of surgical site infections in English hospitals. *J. Hosp. Infect.* 2005;60:93–103. <https://doi.org/10.1016/j.jhin.2004.10.019>.
9. Ardila C, Bedoya-García J, Arrubla-Escobar D. Antibiotic resistance in periodontitis patients: Aa systematic scoping review of randomized clinical trials. *Oral. Dis.* 2023;29:2501–11. <https://doi.org/10.1111/odi.14288>.
10. Sczepanik F, Grossi ML, Casati M, Goldberg M, Glogauer M, Fine N, et al. Periodontitis is an inflammatory disease of oxidative stress: We should treat it that way. *Periodontology.* 2020;84:45–68. <https://doi.org/10.1111/prd.12342>.
11. Li J, Zeng H, Zeng Z. Promising graphene-based nanomaterials and their biomedical applications and potential risks: a comprehensive review. *ACS. Biomater. Sci. Eng.* 2021;7:5363–96. <https://doi.org/10.1021/acsbiomaterials.1c00875>.
12. C Rao, A Sood, K Subrahmanyam, et al. *Angew. Chem. Int. Ed. Engl.* 48 (2009) 7752–77. <https://doi.org/10.1002/anie.200901678>.
13. Avouris P. Graphene: electronic and photonic properties and devices. *Nano. Lett.* 2010;10:4285–94. <https://doi.org/10.1021/nl102824h>.
14. Cai W, Zhu Y, Li X. Large area, few-layer graphene/graphite films as transparent thin conducting electrodes. *Appl. Phys. Lett.* 2009;95:123115 <https://doi.org/10.1063/1.3220807>.
15. Sang M, Shin J, Kim K, Yu KJ. Electronic and thermal properties of graphene and recent advances in graphene based electronics applications. *Nanomaterials.* 2019;9:374 <https://doi.org/10.3390/nano9030374>.
16. Huang X, Yin Z, Wu S, Qi X, He Q, Zhang Q, et al. Graphene-based materials: synthesis, characterization, properties, and applications. *Small.* 2011;7:1876–902. <https://doi.org/10.1002/sml.201002009>.
17. Stankovich S, Dikin DA, Dommett GH, Kohlhaas KM, Zimney EJ, Stach EA, et al. Graphene-based composite materials. *Nature.* 2006;442:282–6. <https://doi.org/10.1038/nature04969>.
18. Lonkar SP, Deshmukh YS, Abdala AA. Recent advances in chemical modifications of graphene. *Nano. Res.* 2015;8:1039–74. <https://doi.org/10.1007/s12274-014-0622-9>.
19. He J, Zhu X, Qi Z, Wang C, Mao X, Zhu C, et al. Killing dental pathogens using antibacterial graphene oxide. *ACS. Appl. Mater. Interfaces.* 2015;7:5605–11. <https://doi.org/10.1021/acsami.5b01069>.
20. Olteanu D, Filip A, Socaci C, Biris AR, Filip X, Coros M, et al. Cytotoxicity assessment of graphene-based nanomaterials on human dental follicle stem cells. *Colloids. Surf. B. Biointerfaces.* 2015;136:791–8. <https://doi.org/10.1016/j.colsurfb.2015.10.023>.
21. Lee JH, Shin YC, Jin OS, Kang SH, Hwang YS, Park JC, et al. Reduced graphene oxide-coated hydroxyapatite composites stimulate spontaneous osteogenic differentiation of human mesenchymal stem cells. *Nanoscale.* 2015;7:11642–51. <https://doi.org/10.1039/c5nr01580d>.
22. Halim A, Luo Q, Ju Y, Song G. A mini review focused on the recent applications of graphene oxide in stem cell growth and differentiation. *Nanomaterials.* 2018;8:736 <https://doi.org/10.3390/nano8090736>.
23. Nizami M, Takashiba S, Nishina Y. Graphene oxide: a new direction in dentistry. *App. Mater. Today.* 2020;19:100576 <https://doi.org/10.1016/j.apmt.2020.100576>.
24. Wei C, Liu Z, Jiang F, Zeng B, Huang M, Yu D. Cellular behaviours of bone marrow-derived mesenchymal stem cells towards pristine graphene oxide nanosheets. *Cell. Prolif.* 2017;50:e12367 <https://doi.org/10.1111/cpr.12367>.
25. Tang LA, Lee WC, Shi H, Wong EY, Sadovoy A, Gorelik S, et al. Highly wrinkled cross-linked graphene oxide membranes for biological and charge-storage applications. *Small.* 2012;8:423–31. <https://doi.org/10.1002/sml.201101690>.
26. Tatavarty R, Ding H, Lu G, Taylor RJ, Bi X. Synergistic acceleration in the osteogenesis of human mesenchymal stem cells by graphene oxide-calcium phosphate nanocomposites. *Chem. Commun.* 2014;50:8484–7. <https://doi.org/10.1039/c4cc02442g>.
27. Matsumoto Y, Koinuma M, Ida S, Hayami S, Taniguchi T, Hatakeyama K, et al. Photoreaction of graphene oxide nanosheets in water. *J. Phys. Chem. C.* 2011;115:19280–6. <https://doi.org/10.1021/jp206348s>.
28. Dimiev AM, Kosynkin DV, Alemany LB, Chaguine P, Tour JM. Pristine graphite oxide. *J. Am. Chem. Soc.* 2012;134:2815–22. <https://doi.org/10.1021/ja211531y>.
29. Otsuka H, Urita K, Honma N, Kimuro T, Amako Y, Kukobat R, et al. Transient chemical and structural changes in graphene oxide during ripening. *Nat Commun.* 2024;15:1708 <https://doi.org/10.1038/s41467-024-46083-4>.
30. Chua CK, Pumera M. Chemical reduction of graphene oxide: a synthetic chemistry viewpoint. *Chem Soc Rev.* 2014;43:291–312. <https://doi.org/10.1039/c3cs60303b>.
31. Lee H, Scherer NF, Messersmith P. Single-molecule mechanics of mussel adhesion. *Proc. Natl. Acad. Sci. USA.* 2006;103:12999–3003. <https://doi.org/10.1073/pnas.060552103>.
32. Lee H, Dellatore SM, Miller WM, Messersmith PB. Mussel-inspired surface chemistry for multifunctional coatings. *Science.* 2007;318:42 6–30. <https://doi.org/10.1126/science.1147241>.
33. Yan Y, Jiang W, Liu L, Wang X, Ding C, Tian Z, et al. Dopamine controls systemic inflammation through inhibition of NLRP3 inflammasome. *Cell.* 2015;160:62–73. <https://doi.org/10.1016/j.cell.2014.11.047>.
34. Jeong KJ, Wang L, Stefanescu CF, Lawlor MW, Polat J, Dohlman CH, et al. Polydopamine coatings enhance biointegration of a model polymeric implant. *Soft. Matter.* 2011;7:8305–12. <https://doi.org/10.1039/c1sm05918a>.
35. Wang Q, Zhang R, Lu M, You G, Wang Y, Chen G, et al. Bioinspired polydopamine-coated hemoglobin as potential oxygen carrier with antioxidant properties. *Biomacromolecules.* 2017;18:1333–41. <https://doi.org/10.1021/acs.biomac.7b00077>.

36. Zhao W, Wang H, Han Y, Wang H, Sun Y, Zhang H. Dopamine/phosphorylcholine copolymer as an efficient joint lubricant and ROS scavenger for the treatment of osteoarthritis. *ACS Appl Mater Interfaces*. 2020;12:51236–48. <https://doi.org/10.1021/acsaami.0c14805>.
37. Li X, Wang T, Luo Y, Asiri AM, Chen S, Sun X. Biomimetic assembly of a polydopamine layer on graphene as an electron gate for fluorescent microrna detection in living cells. *Chembiochem*. 2020;21:801–6. <https://doi.org/10.1002/cbic.201900548>.
38. Jia Z, Shi Y, Xiong P, Zhou W, Cheng Y, Zheng Y, et al. From solution to biointerface: graphene self-assemblies of varying lateral sizes and surface properties for biofilm control and osteo-differentiation. *ACS Appl Mater Interfaces*. 2016;8:17151–65. <https://doi.org/10.1021/acsami.6b05198>.
39. Dreyer DR, Park S, Bielawski CW, Ruoff RS. The chemistry of graphene oxide. *Chem Soc Rev*. 2010;39:228–40. <https://doi.org/10.1039/b917103g>.
40. Liu Y, Ai K, Lu L. Polydopamine and its derivative materials: synthesis and promising applications in energy, environmental, and biomedical fields. *Chem Rev*. 2014;114:5057–115. <https://doi.org/10.1021/cr400407a>.
41. Lee H, Dellatore SM, Miller WM, Messersmith PB. Mussel-inspired surface chemistry for multifunctional coatings. *Science*. 2007;318:426–30. <https://doi.org/10.1126/science.1147241>.
42. Wang Y, Shao Y, Matson DW, Li J, Lin Y. Nitrogen-doped graphene and its application in electrochemical biosensing. *ACS Nano*. 2010;4:1790–8. <https://doi.org/10.1021/nn100315s>.
43. Ci D, Wang N, Xu Y, Wu S, Wang J, Li H, et al. SiO₂@AuAg/PDA hybrid nanospheres with photo-thermally enhanced synergistic antibacterial and catalytic activity. *RSC Adv*. 2024;14:4518–32. <https://doi.org/10.1039/d3ra07607e>.
44. Li Y, Yuan H, von dem Bussche A, Creighton M, Hurt RH, Kane AB, et al. Graphene microsheets enter cells through spontaneous membrane penetration at edge asperities and corner sites. *Proc Natl Acad Sci USA*. 2013;110:12295–12300. <https://doi.org/10.1073/pnas.1222276110>.
45. Alkhouzaam A, Qiblawey H, Khraisheh M. Polydopamine functionalized graphene oxide as membrane nanofiller: spectral and structural studies. *Membranes*. 2021;11:86 <https://doi.org/10.3390/membranes11020086>.
46. Chen FM, Gao LN, Tian BM, Zhang XY, Zhang YJ, Dong GY, et al. Treatment of periodontal intrabony defects using autologous periodontal ligament stem cells: a randomized clinical trial. *Stem Cell Res Ther*. 2016;7:33 <https://doi.org/10.1186/s13287-016-0288-1>.
47. Hynes K, Menicanin D, Han J, Marino V, Mroziak K, Gronthos S, et al. Mesenchymal stem cells from iPS cells facilitate periodontal regeneration. *J Dent Res*. 2013;92:833–9. <https://doi.org/10.1177/0022034513498258>.
48. Liao KH, Lin YS, Macosko CW, Haynes CL. Cytotoxicity of graphene oxide and graphene in human erythrocytes and skin fibroblasts. *ACS Appl Mater Interfaces*. 2011;3:2607–15. <https://doi.org/10.1021/am200428v>.
49. Halim A, Liu L, Ariyanti AD, Ju Y, Luo Q, Song G. Low-dose suspended graphene oxide nanosheets induce antioxidant response and osteogenic differentiation of bone marrow-derived mesenchymal stem cells via JNK-dependent FoxO1 activation. *J Mater Chem B*. 2019;7:5998–6009. <https://doi.org/10.1039/c9tb01413f>.
50. Gurunathan S, Arsalan Iqbal M, Qasim M, Park CH, Yoo H, Hwang JH, et al. Evaluation of graphene oxide induced cellular toxicity and transcriptome analysis in human embryonic kidney cells. *Nanomaterials*. 2019;9:969 <https://doi.org/10.3390/na9070969>.
51. Ku SH, Lee M, Park CB. Carbon-based nanomaterials for tissue engineering. *Adv Healthc Mater*. 2013;2:244–60. <https://doi.org/10.1002/adhm.201200307>.
52. Luo R, Tang L, Zhong S, Yang Z, Wang J, Weng Y, et al. In vitro investigation of enhanced hemocompatibility and endothelial cell proliferation associated with quinone-rich polydopamine coating. *ACS Appl Mater Interfaces*. 2013;5:1704–14. <https://doi.org/10.1021/am3027635>.
53. Bao Y, Yin L, Liu L, Chen L. Acid-sensitive ROS-triggered dextran-based drug delivery system for advanced chemophotodynamic synergistic therapy. *J Biomed Mater Res A*. 2020;108:148–56. <https://doi.org/10.1002/jbm.a.36800>.
54. Bernar A, Gebetsberger JV, Bauer M, Streif W, Schirmer M. Optimization of the alizarin red S assay by enhancing mineralization of osteoblasts. *Int J Mol Sci*. 2022;24:723 <https://doi.org/10.3390/ijms24010723>.
55. Qin H, Zhu C, An Z, Jiang Y, Zhao Y, Wang J, et al. Silver nanoparticles promote osteogenic differentiation of human urine-derived stem cells at noncytotoxic concentrations. *Int J Nanomedicine*. 2014;9:2469–78. <https://doi.org/10.2147/IJN.S59753>.
56. Wei D, Zhang XL, Wang YZ, Yang CX, Chen G. Lipid peroxidation levels, total oxidant status and superoxide dismutase in serum, saliva and gingival crevicular fluid in chronic periodontitis patients before and after periodontal therapy. *Aust Dent J*. 2010;55:70–8. <https://doi.org/10.1111/j.1834-7819.2009.01123.x>.
57. Anusuya S, Mlv P, Lazarus F, Bhavikatti SK, Babrawala IS. Estimation of 8-hydroxy-deoxyguanosine (8-OHdG) in saliva as a marker of oxidative stress in patients with chronic periodontitis: preliminary data. *J Int Acad Periodontol*. 2017;19:95–100.
58. Qiu Y, Wang Z, Owens AC, Kulaots I, Chen Y, Kane AB, et al. Antioxidant chemistry of graphene-based materials and its role in oxidation protection technology. *Nanoscale*. 2014;6:11744–55. <https://doi.org/10.1039/c4nr03275f>.
59. Ju KY, Lee Y, Lee S, Park SB, Lee JK. Bioinspired polymerization of dopamine to generate melanin-like nanoparticles having an excellent free-radical-scavenging property. *Biomacromolecules*. 2011;12:625–32. <https://doi.org/10.1021/bm101281b>.
60. Ming P, Liu Y, Yu P, Jiang X, Yuan L, Cai S, et al. A biomimetic Se-nHA/PC composite microsphere with synergistic immunomodulatory and osteogenic ability to activate bone regeneration in periodontitis. *Small*. 2024;20:e2305490 <https://doi.org/10.1002/sml.202305490>.
61. Garaicoa-Pazmino C, Fretwurst T, Squarize CH, Berglundh T, Giannobile WV, Larsson L, et al. Characterization of macrophage polarization in periodontal disease. *J Clin Periodontol*. 2019;46:830–9. <https://doi.org/10.1111/jcpe.13156>.
62. Zhu H, Tamura A, Zhang S, Terauchi M, Yoda T, Yui N. Mitigating RANKL-induced cholesterol overload in macrophages with β -cyclodextrin-threaded polyrotaxanes suppresses osteoclastogenesis. *Biomater Sci*. 2022;10:5230–42. <https://doi.org/10.1039/d2bm00833e>.
63. Tan J, Zhou L, Xue P, An Y, Luo L, Zhang R, et al. Tumor necrosis factor- α attenuates the osteogenic differentiation capacity of periodontal ligament stem cells by activating PERK signaling. *J Periodontol*. 2016;87:e159–71. <https://doi.org/10.1902/jop.2016.150718>.
64. Cui Y, Hong S, Xia Y, Li X, He X, Hu X, et al. Melatonin engineering M2 macrophage-derived exosomes mediate endoplasmic reticulum stress and immune reprogramming for periodontitis therapy. *Adv Sci*. 2023;10:e2302029 <https://doi.org/10.1002/adv.202302029>.
65. Cheng Z, Kang M, Peng X, Ren L, Xie J, Yuan Q, et al. Self-assembled eutectogel with cell permeation and multiple anti-inflammatory abilities for treating chronic periodontitis. *Adv Mater*. 2025;37:e2412866 <https://doi.org/10.1002/adma.202412866>.
66. Ito AM, Vemula SL, Gupta MT, Giram MV, Kumar SA, Ghosh B, et al. Multifunctional graphene oxide nanoparticles for drug delivery in cancer. *J Control Release*. 2022;350:26–59. <https://doi.org/10.1016/j.jconrel.2022.08.011>.

67. Maleki P, Dinari A, Jahangiri B, Raheb J. In vitro assessments of nanoplexes of polyethylenimine-coated graphene oxide-plasmid through various cancer cell lines and primary mesenchymal stem cells. *PLoS ONE*. 2023;18:e0295822 <https://doi.org/10.1371/journal.pone.0295822>.
68. Fu Y, Yang L, Zhang J, Hu J, Duan G, Liu X, et al. Polydopamine antibacterial materials. *Mater Horiz*. 2021;8:1618–33. <https://doi.org/10.1039/d0mh01985b>.
69. Cao J, Zhang T, Zhu W, Li HB, Shen AG. A cooling-driven self-adaptive and removable hydrogel coupled with combined chemophotothermal sterilization for promoting infected wound healing. *Nanoscale*. 2023;15:11163–78. <https://doi.org/10.1039/d3nr01624b>.
70. He Y, Chen G, Li Y, Li Y, Yi C, Zhang X, et al. Effect of magnetic graphene oxide on cellular behaviors and osteogenesis under a moderate static magnetic field. *Nanomedicine*. 2021;37:102435 <https://doi.org/10.1016/j.nano.2021.102435>.
71. Wu X, Zheng S, Ye Y, Wu Y, Lin K, Su J. Enhanced osteogenic differentiation and bone regeneration of poly(lactic-co-glycolic acid) by graphene via activation of PI3K/Akt/GSK-3 β / β -catenin signal circuit. *Biomater Sci*. 2018;6:1147–58. <https://doi.org/10.1039/C8BM00127H>.
72. Wang Y, Chen Y, Zhou T, Li J, Zhang N, Liu N, et al. A novel multifunctional nanocomposite hydrogel orchestrates the macrophage reprogramming-osteogenesis crosstalk to boost bone defect repair. *J Nanobiotechnology*. 2024;22:702 <https://doi.org/10.1186/s12951-024-02996-2>.
73. Dimiev AM, Alemany LB, Tour JM. Graphene oxide. Origin of acidity, its instability in water, and a new dynamic structural model. *ACS Nano*. 2013;7:576–88. <https://doi.org/10.1021/nn3047378>.
74. Kurapati R, Russier J, Squillaci MA, Treossi E, Ménard-Moyon C, Del Rio-Castillo AE, et al. Dispersibility-dependent biodegradation of graphene oxide by myeloperoxidase. *Small*. 2015;11:3985–94. <https://doi.org/10.1002/sml.201500038>.
75. Kurapati R, Mukherjee SP, Martín C, Bepete G, Vázquez E, Pénicaud A, et al. Degradation of single-layer and few-layer graphene by neutrophil myeloperoxidase. *Angew Chem Int Ed Engl*. 2018;57:11722–7.
76. Bao X, Zhao J, Sun J, Hu M, Yang X. Polydopamine nanoparticles as efficient scavengers for reactive oxygen species in periodontal disease. *ACS Nano*. 2018;12:8882–92. <https://doi.org/10.1021/acsnano.8b04022>.